Temperature-entropy formulation of thermoelectric thermodynamic cycles

H. T. Chua,[1,2,*] K. C. Ng,[2,†] X. C. Xuan,[2] C. Yap,[2] and Jeffrey M. Gordon[3,4,‡]

[1]*Bachelor of Technology Programme, Faculty of Engineering, National University of Singapore, 10 Kent Ridge Crescent, Singapore 119260, Singapore*

[2]*Department of Mechanical Engineering, National University of Singapore, 10 Kent Ridge Crescent, Singapore 119260, Singapore*

[3]*Department of Energy and Environmental Physics, Jacob Blaustein Institute for Desert Research, Ben-Gurion University of the Negev, Sede Boqer Campus 84990, Israel*

[4]*The Pearlstone Center for Aeronautical Engineering Studies, Department of Mechanical Engineering, Ben-Gurion University of the Negev, Beersheva 84105, Israel*

(Received 30 November 2001; published 10 May 2002)

A temperature-entropy formulation is derived for thermoelectric devices. Thermoelectric chiller and generator cycles can then be cast in the same irreversible thermodynamics framework commonly applied to conventional large-scale cooling and power generation equipment, including a transparent identification of the principal energy flows and performance bottlenecks (dissipation). Distinct differences in chiller versus generator mode are highlighted and illustrated with data from commercial thermoelectric units.

DOI: 10.1103/PhysRevE.65.056111 PACS number(s): 05.70.Ln, 84.60.Rb, 85.80.Fi

I. INTRODUCTION

The first and second laws of thermodynamics suggest that plotting the trajectories of thermodynamic cooling and power generation systems in the temperature-entropy (*T-S*) plane should allow the direct identification and quantification of the principal performance variables and sources of dissipation. Indeed, conventional large-scale chillers and heat engines (typically gas or vapor-liquid cycles) are commonly characterized in these terms [1,2]. Recently, the corresponding *T-S* formulation was established for sorption cycles [3–5]. The derivation presented here extends the formalism to thermoelectric cycles, and indicates how other solid-state cycles could be analyzed similarly.

A thermoelectric device, drawn schematically in Fig. 1, can be operated in either chiller or generator mode, between cold and hot reservoirs at temperatures T_c and T_h, respectively. Its entropy fluxes derive from electronic motion and heat conduction, in contrast to the traditional cooling and heat-engine cycles where the entropy fluxes stem primarily from fluid convection.

In analyzing the chiller and generator thermodynamic cycles in the *T-S* plane, one needs to distinguish the entropy fluxes of the working fluid from the additional entropy fluxes in the reservoirs and at the interface with the reservoirs. By isolating the thermoelectric device's internal entropy fluxes, we shall derive and plot the analytic *T-S* relation. This includes the transparent identification of the key heat and work flows, the heat conduction and electrical resistive dissipative losses, and the distinct differences between cooling and heat-engine modes, all supported with data from commercial thermoelectric devices.

*Email address: engcht@nus.edu.sg

†Email address: mpengkc@nus.edu.sg

‡Email address: jeff@menix.bgu.ac.il

II. DERIVATION OF THE *T-S* RELATION

First, we shall note the general entropy flux relations for any thermodynamic cycle at steady state. Then we will proceed to apply them specifically to thermoelectric devices.

We relate to the entropy flux density $\mathbf{J}_s$ (in $\mathrm{W\,m^{-2}\,K^{-1}}$) in a given control volume of the working fluid. $\mathbf{J}_s = S/A$, where S is the entropy flux and A denotes the cross-sectional area. For a thermodynamic cycle at steady state, the relations among (a) $\mathbf{J}_s$, (b) total entropy flux density $\mathbf{J}_{s,\mathrm{tot}}$ that includes the heat exchange between the working fluid and its reservoirs, (c) local temperature T, (d) heat flux density $\mathbf{J}_q$ (in $\mathrm{W\,m^{-2}}$) for the thermal exchange between the working fluid and its reservoirs, (e) rate of internal entropy generation per unit volume σ, and (f) rate of total entropy generation per unit volume σ_{tot} that includes the thermal communication between the working fluid and its reservoirs, are

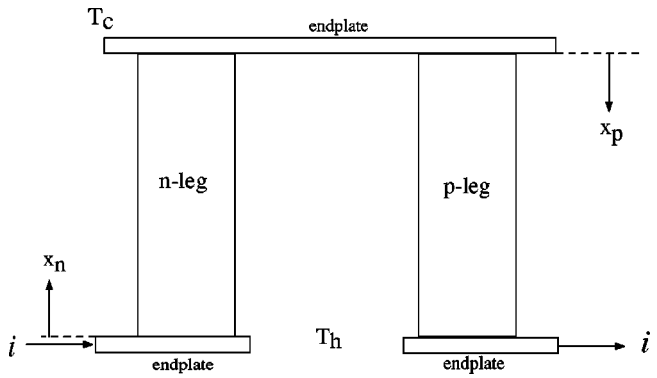

FIG. 1. Schematic representation of a (single-stage) thermoelectric device. The two legs comprise *n*-doped and *p*-doped semiconductors, in thermal contact with hot and cold reservoirs at temperatures T_h and T_c, respectively. In chiller mode, current i is injected (power input), the cooling effect is produced at the cold reservoir, and heat is rejected at the hot reservoir. In generator mode, heat is input at the hot reservoir, rejected at the cold reservoir, and electrical power of current i is produced.

TABLE I. Physical parameters of a single thermoelectric couple [9]. Temperature-dependent properties are taken at the mean operating temperature.

Property	Value for chiller mode	Value for generator mode
Hot reservoir temperature T_h	300 K	360 K
Cold reservoir temperature T_c	270 K	300 K
Length L	1.14×10^{-3} m	1.14×10^{-3} m
Cross-sectional area A	1.96×10^{-6} m^2	1.96×10^{-6} m^2
Thermal conductivity λ	1.70 W m^{-1} K^{-1}	1.60 W m^{-1} K^{-1}
Electrical resistivity R	1.03×10^{-5} Ω m	1.27×10^{-5} Ω m
Seebeck coefficient η	2.07×10^{-4} V K^{-1}	2.21×10^{-4} V K^{-1}
Figure of merit Z	2.45×10^{-3} K^{-1}	2.40×10^{-3} K^{-1}

$$T\nabla\cdot\mathbf{J}_s=-\nabla\cdot\mathbf{J}_q+T\left[\sigma_{\rm tot}-\mathbf{J}_q\cdot\nabla\left(\frac{1}{T}\right)\right]=-\nabla\cdot\mathbf{J}_q+T\sigma, \tag{1}$$

$$\mathbf{J}_s=\mathbf{J}_{s,\rm tot}-\frac{\mathbf{J}_q}{T}. \tag{2}$$

For an adiabatic branch, where $\nabla\cdot\mathbf{J}_q=0$, Eq. (1) reduces to $\nabla\cdot\mathbf{J}_s=\sigma$. For a heat-exchange branch between the working fluid and a reservoir (e.g., for the thermoelectric device, at the junctions between the legs and the endplates), Eq. (1) reduces to

$$T\nabla\cdot\mathbf{J}_s=-\nabla\cdot\mathbf{J}_q. \tag{3}$$

In other words, the net heating or cooling rate is given by the volume integral of $T\nabla\cdot\mathbf{J}_s$.

The entropy fluxes that stem from the (a) heat and mass fluxes and (b) internal dissipation can be measured separately. The heat and mass fluxes, as well as the temperatures, at the entrance and exit to the control volume can also be measured directly. So the entropy fluxes can be calculated at those points. The difference between the entering and exiting entropy fluxes is simply the rate of internal entropy generation.

The thermoelectric cycle comprises two approximately isothermal heat exchange branches (at the interfaces between the legs and the reservoirs) connected by two essentially adiabatic branches. Along the adiabats,

$$\mathbf{J}_s=-\frac{\lambda\nabla T}{T}+\frac{\pi\mathbf{I}}{T}=-\frac{\lambda\nabla T}{T}-\eta\mathbf{I}, \tag{4}$$

$$\sigma_{\rm tot}=\sigma=-\lambda\nabla T\cdot\nabla\left(\frac{1}{T}\right)+\frac{R\mathbf{I}\cdot\mathbf{I}}{T}=\sigma_{\rm cond}+\sigma_{\rm Joule}, \tag{5}$$

where $\mathbf{I}=i/A$ is the electrical current density (in A m^{-2}) with i denoting the (directional) current. The material properties are (a) λ is the thermal conductivity, (b) π is the Peltier coefficient, (c) η is the Seebeck coefficient, and (d) R is the electrical resistivity. The two terms on the right-hand side of Eq. (5) represent the rates of entropy generation (per unit volume) due to heat conduction and electrical resistive (Joule) heating, respectively.

The energy conservation equation that follows from Eqs. (3)–(5) furnishes the equation for the spatial dependence of T,

$$\nabla\cdot(\lambda\nabla T)-T\frac{\partial\eta}{\partial T}\mathbf{I}\cdot\nabla T+T\mathbf{I}\cdot\nabla\eta|_T+R\mathbf{I}^2=0. \tag{6}$$

Equations (1)–(6) embody the T-S (equivalently, T-J_s) relation for thermoelectric cycles, with T and J_s related parametrically via their spatial dependence. J_s denotes $\mathbf{J}_s\cdot\hat{x}$ where $\hat{x}$ is the unit vector along the direction of current flow. An analytic result can be derived if a few approximations that turn out to be accurate for real thermoelectric devices are invoked [6–9]. We select a commercial Bi_2Te_3 thermoelectric module [9] for which the physical parameters are summarized in Table I.

First, current flow and heat conduction are well approximated as one-dimensional (Fig. 1). We track $T(x)$ and J_s along the current's trajectory. The T-J_s graphs developed in Sec. IV clearly show the closed loop (thermodynamic cycle) traced by J_s.

Second, in Eq. (6), the Thomson coefficient term $[T(\partial\eta/\partial T)]$ is usually negligible (i.e., the Seebeck coefficient is well approximated as constant over operating temperature ranges of practical interest). Third, the Seebeck coefficients for the n leg and p leg are approximately equal in magnitude: $\eta_n=-\eta_p\equiv\eta>0$. Fourth, the irreversibility of finite-rate heat transfer at the semiconductor-reservoir interface is viewed as inconsequential (relative to other irreversibilities). Fifth, in considering homogeneous materials, the $\nabla\eta|_T$ term in Eq. (6) is also negligible.

Equation (6) then reduces to

$$\lambda\frac{d^2T}{dx^2}=-R\mathbf{I}^2. \tag{7}$$

With the boundary conditions indicated in Fig. 1, for thermoelectric legs of length $L(0\leqslant x\leqslant L)$, the solution to Eq. (7) is

$$T_n(x)=T_h-\frac{x\Delta T}{L}+\frac{\mathbf{I}^2RL^2}{2\lambda}\left[\frac{x}{L}-\left(\frac{x}{L}\right)^2\right] \quad \text{on the } n \text{ leg} \tag{8a}$$

and

$$T_p(x)=T_c+\frac{x\Delta T}{L}+\frac{\mathbf{I}^2RL^2}{2\lambda}\left[\frac{x}{L}-\left(\frac{x}{L}\right)^2\right] \quad \text{on the } p \text{ leg,} \tag{8b}$$

where $\Delta T=T_h-T_c$.

The solutions to Eq. (4) for the entropy flux densities on the n leg and p leg are

$$\mathbf{J}_{s,n}(x)=\frac{\mathbf{I}^2RL\left[\frac{x}{L}-\frac{1}{2}\right]+\frac{\lambda\Delta T}{L}}{T_n(x)}\hat{x}-\eta\mathbf{I}, \tag{9a}$$

$$\mathbf{J}_{s,p}(x)=\frac{\mathbf{I}^2RL\left[\frac{x}{L}-\frac{1}{2}\right]-\frac{\lambda\Delta T}{L}}{T_p(x)}\hat{x}+\eta\mathbf{I}, \tag{9b}$$

where $\mathbf{J}_{s,n}(x)$ is negative and $\mathbf{J}_{s,p}(x)$ is positive. Equations (8) and (9) represent the desired (parametric) temperature-entropy relation, which will be explored in Sec. IV.

III. THERMODYNAMIC PERFORMANCE VARIABLES

The heat flux densities at the cold and hot reservoirs are, respectively,

$$q_c=T_c|\mathbf{J}_{s,p}(0)-\mathbf{J}_{s,n}(L)|=2\eta\mathbf{I}T_c\mp\mathbf{I}^2RL\mp\frac{2\lambda\Delta T}{L}, \tag{10a}$$

$$q_h=T_h|\mathbf{J}_{s,p}(L)-\mathbf{J}_{s,n}(0)|=2\eta\mathbf{I}T_h\pm\mathbf{I}^2RL\mp\frac{2\lambda\Delta T}{L}, \tag{10b}$$

where (a) all heat and work flows are defined as positive, and (b) the upper sign denotes chiller mode and the lower sign generator mode. From the first law, the electrical power density P (input power in chiller mode, and power produced in generator mode) is

$$P=q_h-q_c=2\eta\mathbf{I}\Delta T\pm2\mathbf{I}^2RL. \tag{11}$$

Common measures of conversion efficacy are the coefficient of performance $\mathrm{COP}=q_c/P$ for chillers and efficiency $\varepsilon=P/q_h$ for heat engines. An instructive way to plot the thermodynamic performance is (a) COP against cooling rate for chillers, and (b) efficiency against power output for heat engines [1,2,10]. These are plotted in Fig. 2, with the abscissa variable normalized to its maximum value in order to exhibit both useful effects on the same graph. Four points are noted on each curve: (1) A represents the vanishing COP or efficiency in the low-current limit; (2) B represents the maximum COP or efficiency; (3) C represents the maximum cooling rate or output power; and (4) D represents the vanishing COP or efficiency in the high-current limit.

Thermoelectric quality is often gauged by the material's figure of merit, $Z=\eta^2/(R\lambda)$ (units of K^{-1}), as reflected in the extrema of the performance variables,

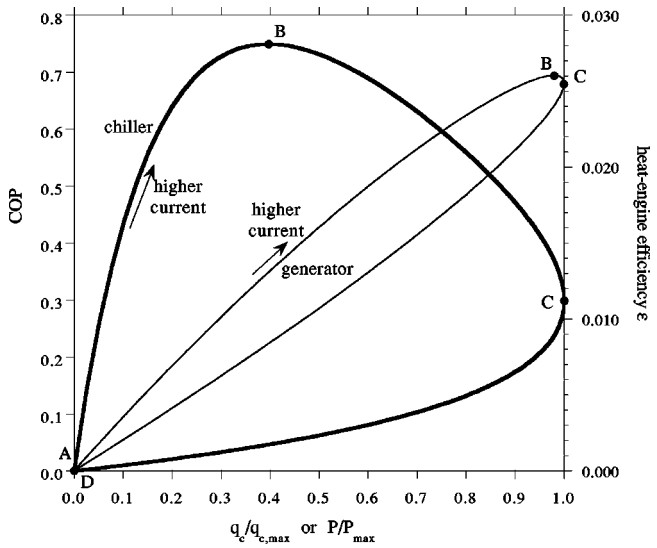

FIG. 2. Characteristic performance curves of the thermoelectric cycles. COP is plotted against cooling rate normalized to its maximum value (for chiller mode). Heat engine efficiency is plotted against the power output normalized to its maximum value (for generator mode). Both curves vanish in the limits of low (A) and high (D) current due to the opposite trends of heat leak and electrical resistive irreversibilities. There are distinct points of (1) maximum COP or efficiency (B), and (2) maximum cooling rate or power output (C). The device properties are noted in Table I.

$$\mathrm{COP}_{\max}=-\frac{1}{2}+\left(\frac{\overline{T}}{\Delta T}\right)\left(\frac{\sqrt{1+Z\overline{T}}-1}{\sqrt{1+Z\overline{T}}+1}\right)$$

$$\text{where } \overline{T}=(T_h+T_c)/2, \tag{12}$$

$$q_{c,\max}=\frac{\lambda}{L}(ZT_c^2-2\Delta T), \tag{13}$$

$$T_{c,\min}=\frac{\sqrt{1+2ZT_h}-1}{Z} \tag{14}$$

for the chiller, and

$$\varepsilon_{\max}=\frac{\Delta T(\sqrt{1+Z\overline{T}}-1)}{T_c+T_h\sqrt{1+Z\overline{T}}}, \tag{15}$$

$$P_{\max}=\frac{Z(\Delta T)^2\lambda}{2L} \tag{16}$$

for the generator.

IV. TEMPERATURE-ENTROPY PLOTS

Figure 3 constitutes the temperature-entropy (actually T-J_s) plots for the operating points of the thermoelectric chiller highlighted in Fig. 2. The extra point E refers to maximizing the thermal lift ΔT, and is considered at the same fixed T_h as the other graphs (i.e., minimum attainable T_c). Figure 4 illustrates the graphic identification of the principal

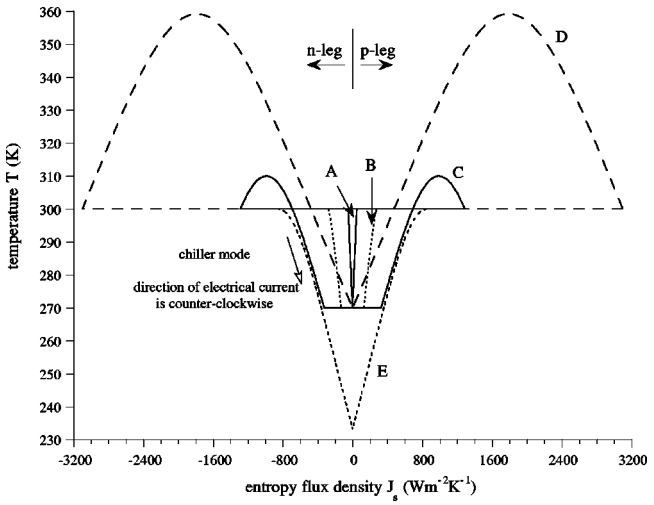

FIG. 3. T-J_s diagrams for the thermoelectric chiller at five operating points. The ordinate is not extended down to zero in order to display sufficient detail for all curves. A represents zero cooling rate and zero COP in the low-current limit. B represents maximum COP. C represents maximum cooling rate. D represents zero cooling rate and zero COP in the high-current limit. E represents minimum T_c at fixed T_h (at zero cooling rate and zero COP).

energy flows at maximum COP and maximum cooling rate. Figures 5 and 6 comprise corresponding graphs for the thermoelectric generator. Performance figures are summarized in Tables II and III.

The rectangles subtended by the hot and cold isotherms represent the respective heat transfer densities q_h and q_c. The areas beneath the adiabats represent dissipation. The area enclosed by the full cyclic T-J_s trajectory (at $T \leqslant T_h$) is the dissipationless (nominally reversible) power density P_{rev}: minimum power input in the chiller mode, and maximum power output in the generator mode. The actual power density, $P = q_h - q_c$, is hence the sum of the area enclosed by the T-J_s path and the area under the adiabats.

The T-J_s graph, together with the first law, also provides a clear interpretation of the Peltier thermoelectric power density $2|\mathbf{I}|\eta\Delta T$. Before formulating the governing equations, we know from the physical picture that the Peltier power should not depend on the electrical resistive dissipation, and should differ from the reversible power only due to the heat conduction irreversibility. q_h can be expressed in two equivalent forms,

$$q_h = q_c + 2|\mathbf{I}|\eta\Delta T \pm 2\int T\sigma_{\mathrm{Joule}}dx \tag{17}$$

and

$$q_h = q_c + P = q_c + P_{\mathrm{rev}} \pm 2\int T\sigma_{\mathrm{cond}}dx \pm 2\int T\sigma_{\mathrm{Joule}}dx. \tag{18}$$

Hence $2|\mathbf{I}|\eta\Delta T = P_{\mathrm{rev}} \pm 2\int T\sigma_{\mathrm{cond}}dx$, which confirms the physical picture noted above. (19)

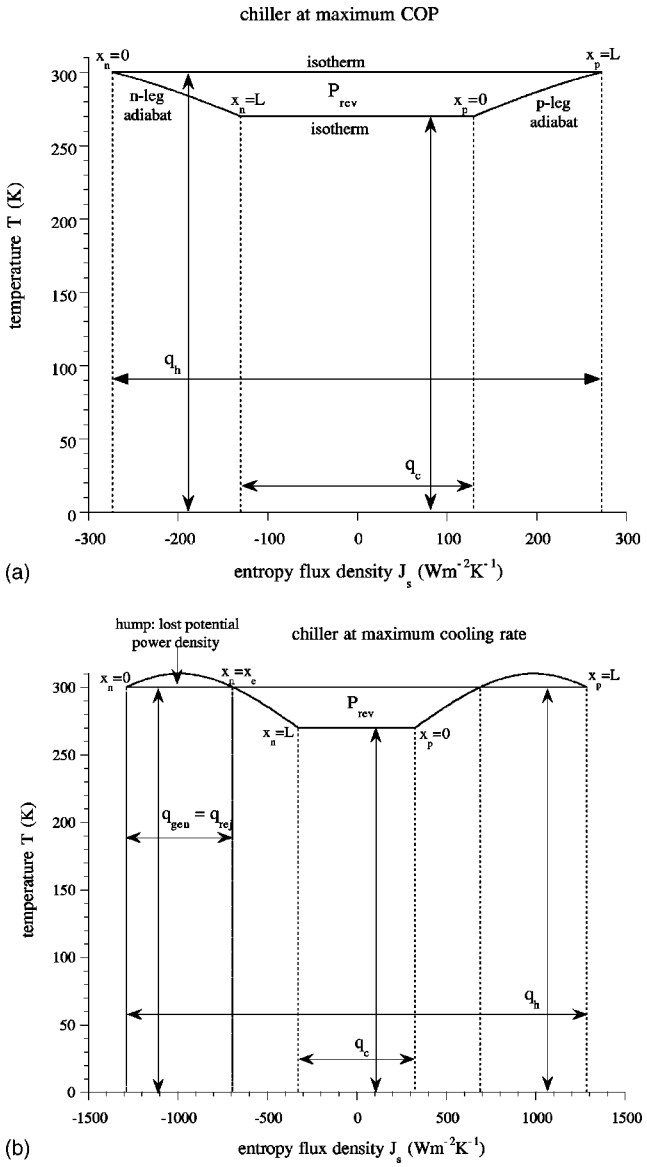

FIG. 4. Graphic identification of the principal energy flows in chiller mode: (a) Maximum COP. (b) Maximum cooling rate.

In the hypothetical reversible (Carnot) limit, the adiabats become isentropes, as thermal and electrical resistance losses vanish (i.e., the T-J_s trajectories reduce to rectangles), for which $\mathrm{COP}_{\mathrm{Carnot}} = T_c/\Delta T$, and $\varepsilon_{\mathrm{Carnot}} = \Delta T/T_h$. In cooling mode, maximum-COP operation is the trajectory that most closely approaches the Carnot cycle. But the irreversibilities are so large that even the best commercial thermoelectric units reach only a small fraction of $\mathrm{COP}_{\mathrm{Carnot}}$ (see Table II). In the opposite extreme of zero COP (points A, D, and E in Fig. 3), the two adiabats intersect at the cold isotherm and the area of the q_c rectangle vanishes.

For the heat engine, the distinctions are less striking. The points of vanishing efficiency occur where the areas under the hot and cold isotherms are equal; and the fact that the maximum-efficiency point is closer to the Carnot cycle than other operating points is less easy to discern.

The relative weights of heat conduction and electrical resistance losses are strongly dependent on the current. In heat

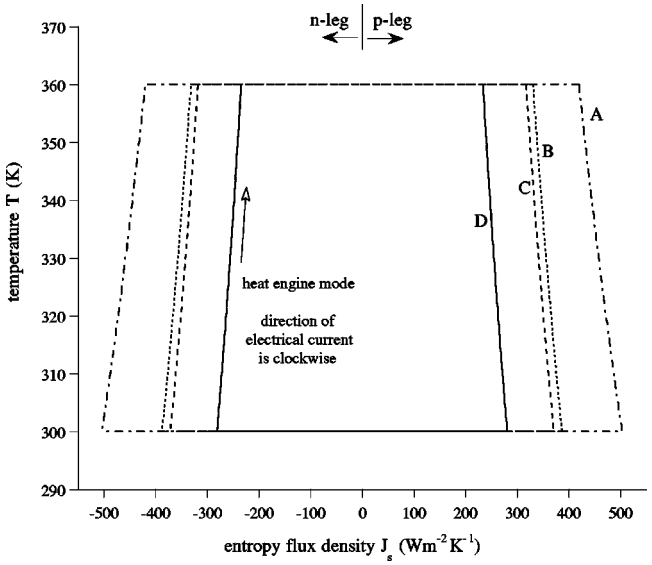

FIG. 5. T-J_s diagrams for the thermoelectric generator at four operating points. The ordinate is not extended to zero in order to display sufficient detail for all curves. A represents zero power and zero efficiency in the zero-current limit. B represents maximum efficiency. C represents maximum power. D represents zero power and zero efficiency in the high-current limit.

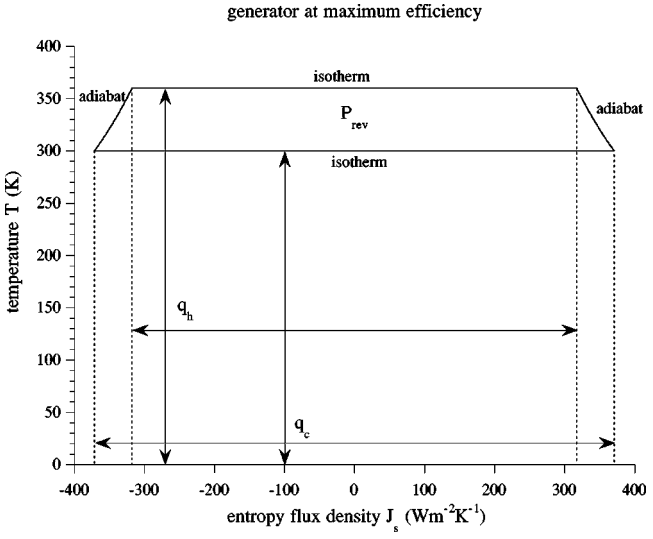

FIG. 6. Graphic identification of the principal energy flows for the generator at maximum efficiency.

engine mode, where relatively low currents are generated, heat conduction losses dominate. In chiller mode, where far higher currents are injected, electrical resistive losses govern (see Tables II and III).

The high-current regime encountered only in chiller mode includes a distinctly different dynamic in the vicinity of the maximum cooling rate operation, apparent from the T-J_s trajectories, refer to Fig. 4(b). Because of the limited rate at which the thermoelectric can conduct away the heat generated by electrical resistance at these elevated current levels, ''humps'' appear in which the local temperature exceeds T_h. The temperature-entropy formulation provides a straightforward identification of the individual contributions of resistive heating, heat conduction, heat rejection, and lost available work, as follows.

Consider the n-leg length x_e over which $T(x) \geqslant T_h$, with $0 \leqslant x_e \leqslant L$. (The analysis is symmetric for the p leg but with the ''hump'' regime starting from the point $x_p = L$ rather than $x_n = 0$). From Eq. (8a),

$$x_e = L - \frac{2\lambda \Delta T}{\mathbf{I}^2 RL}. \tag{20}$$

This regime constitutes a sort of subcycle that produces no cooling, while generating electrical resistive heating that is rejected completely at the hot reservoir. (In fact, the condition of maximum ΔT—point E in Fig. 3—corresponds to requiring that $x_e = 0$ at $q_c = 0$.)

The (dissipative) heat generation density in this region in each leg is

$$q_{\text{gen}} = \mathbf{I}^2 R x_e = \mathbf{I}^2 RL - \frac{2\lambda \Delta T}{L} \tag{21}$$

and represents the extra input power needed to drive the chiller at the elevated cooling rate. This is emblematic of the universal tradeoff in chillers between COP and cooling rate [1]: some excess installed cooling capacity is required (in this case extra thermoelectric length) in order to reap the benefit of maximum COP operation.

The heat rejection density along this segment is simply the corresponding rectangle below the hot isotherm

$$q_{\text{rej}} = T_h [J_s(x_e) - J_s(0)] = \mathbf{I}^2 RL - \frac{2\lambda \Delta T}{L}. \tag{22}$$

Since $q_{\text{gen}} = q_{\text{rej}}$, no cooling power is produced in this subcycle. Furthermore, the area between the adiabat and the hot isotherm (i.e., the area of the ''hump'') must then be precisely the lost potential work due to heat conduction

TABLE II. Performance summary of the thermoelectric chiller. $\text{COP}_{\text{Carnot}} = 9$.

Operating point	Current (A)	Cooling power (W)	COP	Electrical resistive dissipation $2\int T\sigma_{\text{Joule}} dV$ (W)	Heat conduction dissipation $2\int T\sigma_{\text{cond}} dV$ (W)
A	1.73	0	0	0.036	0.019
B	3.43	0.14	0.75	0.14	0.020
C	9.36	0.35	0.30	1.05	0.072
D	16.99	0	0	3.45	0.56
E	8.08	0	0	0.78	0.13

TABLE III. Performance summary of the thermoelectric generator. $\varepsilon_{\text{Carnot}}=0.167$.

Operating point	Current (A)	Output power (W)	Efficiency	Electrical resistive dissipation $2\int T\sigma_{\text{Joule}}dV$ (W)	Heat conduction dissipation $2\int T\sigma_{\text{cond}}dV$ (W)
A	0	0	0	0	0.0600
B	0.77	0.0117	0.0261	0.0088	0.0600
C	0.90	0.0119	0.0255	0.0120	0.0600
D	1.79	0	0	0.0475	0.0602

$$q_{\text{lost}}=-\lambda\int_0^{x_e}T\nabla T\cdot\nabla\left(\frac{1}{T}\right)dx. \tag{23}$$

Another way to verify this claim follows from Eq. (19). The subcycle generates no Peltier power; hence the lost available power is exactly the thermal conductive dissipation.

There is a complementary subcycle between the humps in Fig. 4(b), i.e., in the region $x_e\leqslant x_n\leqslant L$ (and its *p*-leg complement), that can be viewed as an ostensibly autonomous cooling cycle. The performance equations noted above apply, but with the effective leg length taken as $L-x_e$ (rather than L). This complementary subcycle has a higher COP since it produces the same cooling power at reduced input power. This is an equivalent view of the tradeoff noted above between COP and the installed cooling capacity.

V. QUALIFICATION

The temperature and spatial dependencies of the Seebeck coefficient have been treated as negligible—an adequate approximation for most commercial thermoelectric devices of practical interest [6–9]. In the rigorous treatment where these effects are accounted for [in Eqs. (4)–(6)], the local temperatures are distorted from their parabolic profiles [Eq. (8)], and the thermal conduction and electrical resistive losses are affected by their spatial and local temperature dependencies.

Furthermore, the constant horizontal translation of the adiabats in the T-J_s diagrams—that stems from the $\eta\mathbf{I}$ term in Eq. (9)—will then depend on both temperature and position. The qualitative features of the T-J_s graphs remain unaltered, including the identification of the principal energy flows and of dissipation with areas subtended on the T-J_s plots, but the T-J_s trajectories can no longer be expressed analytically.

VI. CONCLUSIONS

Thermoelectric cycles are especially didactic because, to an excellent approximation, their performance trajectories can be solved analytically. The temperature-entropy formulation derived here for thermoelectric devices offers not only a complementary physical-insight approach for their thermodynamic analysis, but also unifies the understanding of their performance with that of a broad spectrum of conventional cooling and heat engine cycles.

The formalism derived here is in principle equally well applicable to other solid-state cycles, e.g., thermionic chillers and generators [11]. However, the analysis is then more complex, and the nominal equation of state that allows us to relate temperature and entropy is less amenable to analytic solution.

Formulating thermodynamic performance in temperature-entropy terms grants a graphic interpretation of the key energy flows, and facilitates distinguishing where performance bottlenecks lie. The trajectories of thermoelectric chillers in the vicinity of their maximum cooling rate exemplify this point, with the clear identification of lost available work, electrical resistive heating, and heat conduction as well as how they enter the total energy balance. The temperature-entropy view of the high-current regime accessible only in cooling mode thus highlights a fundamental difference in chiller versus heat engine operation.

[1] J. M. Gordon and K. C. Ng, *Cool Thermodynamics* (Cambridge International Science Publishing, Cambridge, UK, 2000).
[2] J. M. Gordon and M. Huleihil, J. Appl. Phys. **72**, 829 (1992).
[3] H. T. Chua, H. K. Toh, A. Malek, K. C. Ng, and K. Srinivasan, Int. J. Refrig. **23**, 491 (1999).
[4] H. T. Chua, H. K. Toh, and K. C. Ng, J. Appl. Phys. **88**, 446 (2000).
[5] H. T. Chua, K. C. Ng, A. Malek, and N. M. Oo, J. Appl. Phys. **89**, 5151 (2001).
[6] H. Goldsmid, *Electronic Refrigeration* (Pion, London, 1986).
[7] D. M. Rowe, *Handbook of Thermoelectrics* (CRC, Boca Raton, FL, 1986).
[8] A. Miner, A. Majumdar, and U. Ghoshal, Appl. Phys. Lett. **75**, 1176 (1999).
[9] Melcor Thermoelectric Coolers, Model CP1.4-127-045L, from the company's homepage www.melcor.com (2001).
[10] J. M. Gordon, Am. J. Phys. **59**, 551 (1991).
[11] G. D. Mahan, J. O. Sofo, and M. Bartkowiak, J. Appl. Phys. **83**, 4683 (1998).